

Scientific Research Associates, inc.

50 Nye Road, P.O. Box 1058
Glastonbury, Connecticut 06033
(203) 659-0333

Report R87-900063-F

SOLID ROCKET MOTOR AFT FIELD JOINT
FLOW FIELD ANALYSIS

Jayant S. Sabnis
Howard J. Gibeling
Henry McDonald

(NASA-CR-179288)	SOLID ROCKET MOTOR AFT	N88-24675
FIELD JOINT FLOW FIELD ANALYSIS Final		
Technical Report (Scientific Research		
Associates) 37 p	CSCI 21H	Unclas
	G3/20	0097767

Final SRA Technical Report
Prepared under Contract NAS8-36185

Prepared for
National Aeronautics and Space Administration
George C. Marshall Space Flight Center

September 1987

Introduction

The internal flow field plays an important role in numerous aspects of the design and operation of a solid propellant rocket booster, such as is used in the current shuttle. During design, accurate predictions of the internal flow field are needed to properly estimate motor case insulator requirements, and thereby avoid performance penalties due to excessive inert weight. Under-estimation of insulator thickness has an even greater penalty, as it can result in burnthrough of the motor case and failure of the booster during flight. Pathological flow problems in slots, seals and around inhibitors can create erosion and ablation problems which must be eliminated, and internal flow predictions can give valuable insights into these potential problems.

The capability for predicting the internal flow field and the associated particle history in the rocket motor is also essential to motor performance, nozzle erosion, motor stability and modeling of the erosive burning characteristics of solid rocket propellants. Analysis of the rocket's internal flow field using the techniques of Computational Fluid Dynamics (CFD) is frequently the only feasible means for evaluating other motor phenomena not measurable through static motor tests.

Predictive techniques used commonly at present involve the use of inviscid methods which will be obviously inadequate as the flow transitions to turbulent regime. Techniques estimating the chamber mean flow from experimental data and correlations of one- or two-dimensional inviscid core flow calculations with boundary layer corrections to the mean flow estimated iteratively require the division of the flow into an inviscid region and a boundary layer. In most cases of practical interest, such as in the vicinity of the slots at the segment joint, such a division is not possible and the boundary layer approximations are not valid. Hence, a more general approach for flow field prediction is needed.

Under Contract F04611-83-C-0003 with the Air Force Rocket Propulsion Laboratory, a program was initiated to accurately model the core and near wall regions of the rocket internal flow field, including slots, inhibitors and the nozzle. An existing SRA Navier-Stokes computer program (MINT) has been used to simulate the two-dimensional (axisymmetric) steady state flow of a nonreacting ideal gas in a cylindrical port cold flow model (Refs. 1-2). The computer program was modified to model the massive wall-blowing necessary to simulate

the surface of a burning solid propellant. Geometric capabilities of this computer program were enhanced to accommodate rocket motor geometries with radial slots and restrictors. Preliminary computed results show good agreement with the available experimental data from cold flow experiments on the axial velocity profile in the near wall region. This effort has demonstrated the value of Navier-Stokes predictive models for application to solid propellant rocket motor internal flows. Under the present contract, this code was extended to three dimensions and applied to the simulation of axisymmetric as well as asymmetric flow field in the vicinity of the aft field joint in the space shuttle solid rocket booster (SRB).

Analysis

The internal flow field in the solid rocket motor chamber was simulated by numerical solution of the ensemble-averaged Navier-Stokes equations in a body-fitted, cylindrical polar coordinate system. The equations to be solved are the continuity, momentum conservation, energy conservation and the turbulence model equations. The governing partial differential equations were formulated in conservation form by application of a Jacobian transformation to the equations in a cylindrical-polar coordinate. An outline of the transformation as well as the transformed system of equations have been presented in Ref. 1. The vector form of the equations is described below.

The continuity equation is written as

$$\frac{\partial \rho}{\partial t} + \nabla \cdot \rho \vec{U} = 0 \quad (1)$$

The momentum conservation equation is

$$\frac{\partial(\rho \vec{U})}{\partial t} + \nabla \cdot (\rho \vec{U} \vec{U}) = -\nabla p + \nabla \cdot \underline{\underline{\tau}} \quad (2)$$

where $\underline{\underline{\tau}}$ is the stress tensor (molecular and turbulent) written in cylindrical-polar coordinates.

The energy conservation equation is written as

$$\frac{\partial(\rho h)}{\partial t} + \nabla \cdot (\rho \vec{U} h) = \frac{Dp}{Dt} - \nabla \cdot \vec{q} + \phi \quad (3)$$

where ϕ is the viscous dissipation per unit volume and \vec{q} is the heat flux vector. The stress tensor, given by

$$\tau_{ij} = 2\mu_{\text{eff}} e_{ij} - \frac{2}{3} \mu_{\text{eff}} \nabla \cdot \vec{U} \delta_{ij} \quad (4)$$

where the rate of strain tensor, e_{ij} , is given by

$$e_{ij} = \frac{1}{2} \left(\frac{\partial u_i}{\partial x_j} + \frac{\partial u_j}{\partial x_i} \right) \quad (5)$$

The dissipation rate, ϕ , is expressed as

$$\phi = \mu_{\text{eff}} \left[2e_{ij}e_{ij} - \frac{2}{3} (\nabla \cdot \vec{U})^2 \right] \quad (6)$$

The effective viscosity, μ_{eff} , is the sum of the molecular and turbulent viscosities

$$\mu_{\text{eff}} = \mu + \mu_T \quad (7)$$

The turbulent viscosity, μ_T , is obtained from the turbulence model. The heat flux vector, \vec{q} , is given by

$$\vec{q} = -(\kappa + \kappa_T) \nabla T \quad (8)$$

where κ and κ_T are molecular and turbulent thermal conductivities, respectively. In the present analysis, κ and κ_T are obtained assuming constant molecular and turbulent Prandtl numbers Pr and Pr_T , i.e.

$$\kappa = \frac{\mu C_p}{Pr}$$

(9)

$$k_T = \frac{\mu_T C_p}{Pr_T}$$

The turbulence model used under the present effort is a transitional two-equation (k - ϵ) model discussed by Jones and Launder (Ref. 3), which is a modified form of the k - ϵ turbulence model originally developed by Harlow and Nakayama (Ref. 4). The modifications devised by Jones and Launder allow the k - ϵ model to be utilized throughout the viscous sublayer without any wall function assumption. Further details of the turbulence model are available in Refs. 1 and 3.

The numerical procedure used to solve the governing equations is a consistently split linearized block implicit (LBI) scheme of Briley and McDonald (Ref. 5). The method centers around the use of a formal linearization technique adapted for the integration of initial value problems. The governing equations are replaced by an implicit time difference approximation. Terms involving nonlinearity at the implicit time level are linearized by Taylor series expansion in time about the solution at the known time level, and spatial difference approximations are introduced. The result is a system of multidimensional coupled linear difference equations for the dependent variables at the implicit time level. To solve these difference equations, the Douglas-Gunn (Ref. 6) procedure for generating alternating direction implicit (ADI) schemes as perturbations of fundamental implicit difference schemes is introduced. This technique leads to systems of coupled linear difference equations having block-banded matrix structure which can be solved efficiently by standard block elimination methods.

The linearization technique permits the solution of coupled nonlinear equations in one space dimension by a one-step noniterative scheme. Since no iteration is required to compute the solution for a single time step and only moderate effort is required for solution of the implicit difference equations, the method is computationally efficient; this efficiency is retained for the multidimensional problems by using ADI techniques. The method is also economical in terms of computer storage, in its present form requiring only two time levels of storage for each dependent variable. Further details of the LBI scheme are available in Refs. 5 and 7.

Application and Results

The analysis discussed above was incorporated into the MINT (Multi-dimensional Implicit Navier-Stokes Time-Dependent) code and used by SRA under Contract FO4611-83-C-0003 with the Air Force Rocket Propulsion Laboratory to simulate the steady state flow field in a cylindrical port cold-flow model. The code was also used subsequently to simulate the internal flow in a cold-flow model with a radial slot. The results of this calculation and comparison with experimental data are available in Ref. 2. Under the present contract, the MINT code was used to simulate the internal flow in the vicinity of the aft field joint slot of the space shuttle solid rocket booster (SRB). Calculations included simulation of axisymmetric flow in the chamber to estimate the possible over-pressure at the joint, as well as asymmetric three-dimensional flow in the chamber to estimate the circumferential flow and pressure distribution at the joint caused by pressure asymmetry at the outflow (which could be caused by a canted nozzle) and failure of a section of the castable inhibitor.

A schematic diagram of the computational domain for the axisymmetric case is presented in Fig. 1. While the region of interest is the vicinity of the slot, it is essential to locate the inflow and the outflow boundaries sufficiently far away from the slot in an attempt to keep the flow field in the region of interest free from the assumptions/approximations made at these boundaries. For this reason the inflow and outflow boundaries have been located about 12' away from the slot in either direction while the slot width is only 1.5". The calculations for the axisymmetric simulation were initiated from a quiescent state with pressure and temperature corresponding to the stagnation conditions for the chamber. The mass influx at the boundaries of the computational domain representing the grain surface was specified to be a product of a "permeability factor" and the difference between a specified "plenum pressure" and the static pressure at the boundary. The plenum pressure was set to equal the chamber stagnation pressure, thereby resulting in no mass influx at the initial condition. At the inflow boundary, linear extrapolation of static pressure was used as a boundary condition and the axial velocity at the centerline was computed from the chamber stagnation pressure and the static pressure at the centerline. The axial and radial velocities at all other locations on the inflow boundary were computed using the centerline axial velocity and the

velocity profiles obtained from the inviscid rotational flow analysis of Culick (Ref. 8). All dependent variables except pressure were extrapolated at the outflow boundary. The static pressure at the outflow boundary was gradually lowered, resulting in mass efflux from the domain and reduction in the static pressure in the chamber. The reduced static pressure in the chamber started mass influx from the inflow boundary, as well as the boundaries representing the grain surface. After a flow field was established in the domain, the boundary condition at the grain surface was changed to specify the actual mass flux computed from data on grain regression rate, etc. The static pressure at outflow was adjusted to obtain the desired mass flow at the inflow boundary and the solution procedure marched in time to obtain the steady-state solution.

For the three-dimensional calculations, the computational domain included the same segment length as used in the axisymmetric calculations. In the circumferential direction, a 180° section ($-90^\circ \leq \theta \leq +90^\circ$) of the SRB chamber was included. The initial flow field for the three-dimensional calculations was obtained from the converged solution for the axisymmetric calculations. The appropriate boundary conditions were then changed to introduce the asymmetry and the solution procedure marched in time to obtain the final solution.

Computational Grid

The grid generation technique used to generate a grid of the computational domain is similar to that discussed by Oh (Ref. 9). Every physical location which must coincide with a grid point is designated as a "cluster point". Examples of such locations in the axial direction are the two faces of the slot and in radial direction they would be the grain radius, the beginning of the inhibitors, etc. Complementary error functions are used to distribute the grid points subject to the constraints of the cluster points. Figures 2 and 3 show the grid spacing in the radial and the axial direction, respectively, plotted in the computational space. Since it is necessary to resolve the flow field near the solid surfaces as accurately as possible, a high degree of mesh stretching has been used.

These figures show the degree of mesh stretching used in the calculations. It can be seen, for example, from Fig. 3 that the axial grid spacing at the aft edge of the slot is 0.001" while that near the outflow boundary is 10". The

radial grid distribution utilized 95 grid points while 155 grid points were used along the axial direction. The slot width of 1.5" was resolved using 55 grid points while 40 grid points were used between the inflow boundary and the beginning of the slot, and 60 grid points were used between the aft edge of the slot and the outflow boundary. Figure 4 shows the computational grid used in the two-dimensional calculation for the entire domain in the r-z plane, while the details of the grid in the vicinity of the slot exit are presented in Fig. 5. The grid for the three-dimensional calculations utilized 49 equally spaced points along the circumferential direction. The grid distribution in the r-z plane for the three-dimensional calculations was identical to the one used in the axisymmetric calculations. The total number of grid points for three-dimensional calculations was, thus, 721,525.

Axisymmetric Flow Simulation

The internal flow in an axisymmetric configuration was simulated to study the flow in the vicinity of the slot and to evaluate whether the small slot width along with the absence of an inhibitor on one propellant surface in the slot would result in the pressure at the joint being significantly above the mean chamber pressure. In addition, the flow field obtained for this case was to be used to generate the initial flow field for the three-dimensional flow simulation. The converged solution for the axisymmetric case was obtained in approximately 450 iterations, with each time step requiring approximately 2 seconds of CPU time on a CRAY X-MP. The pressure distribution in the vicinity of the slot is shown in Figs. 6 and 7. Figure 6 shows the pressure distribution along with an outline of the computational domain while Fig. 7 shows a close-up of the region in the vicinity of the slot. The reference pressure for the calculations was 900 psi and thus the over-pressure at the joint (i.e., location in the slot at maximum distance from the centerline) was only about 10 psi above the chamber pressure. The high gas velocity at the slot exit creates a low pressure region at the aft-edge of the slot (as can be seen from Fig. 8) and also creates a region of reverse axial flow near the wall. In Fig. 9, velocity vectors in the vicinity of the slot exit are shown which illustrate this phenomenon. The magnitude of the reversed axial velocity was found to be about 10% of the velocity at the centerline. This region of reversed flow was found to extend about 5 slot widths along the axial

direction, as can be seen from Fig. 10, where streak lines in the vicinity of the slot exit are shown.

Three-Dimensional Flow Simulation

Two cases with an asymmetric flow field in the SRB chamber were simulated under the present contract. The objective of the three-dimensional flow simulation was to estimate the extent of circumferential flow and pressure gradients present at the bottom of the slot, as these parameters are needed in the analysis of the thermal/fluid environment sustained by the joint components. In both cases, the asymmetry in the flow was to be caused by an asymmetric boundary condition. In Case I, the asymmetry was assumed to be an asymmetric pressure imposed at the outflow boundary of the computational domain. This condition could exist in practice, for example, by a canted nozzle in the SRB. In Case II, the asymmetry was assumed to be a result of a failure of a part of the castable inhibitor in the slot. During the simulation of this case, a 7.5° section of the castable inhibitor at $\theta = +90^\circ$ was assumed to be removed, thereby generating an asymmetric flow in the slot.

The results of the calculations for the two cases are presented in Figs. 11 through 25 and discussed below. It should be noted that Figs. 11 through 25 indicate the grid to be $48 \times 49 \times 53$ rather than $95 \times 49 \times 155$. The reason behind this is that, while the computations were performed on a $95 \times 49 \times 155$ grid, the data had to be culled selectively to avoid exceeding the memory of the graphics workstation. Hence, the plot-file used consisted of approximately every alternate grid point in the radial direction and every third point along the axial direction.

Case I Results: The asymmetric pressure distribution imposed at the outflow boundary was obtained by varying the static pressure at the outflow boundary linearly along the diameter of the outflow plane. The pressure distribution at the inflow boundary was axisymmetric, as can be seen from Fig. 11. The pressure distribution at the outflow boundary is shown in Fig. 12. The magnitude of the pressure drop along the diameter at the outflow plane was approximately 9.5 psi. The resultant asymmetry in the axial velocity can be seen from Fig. 13, which shows a shift in the axial velocity peak towards the low pressure side. The pressure and axial velocity distribution approximately

one diameter upstream of the outflow boundary are presented in Figs. 14 and 15, respectively. At this location, the axial velocity distribution appears fairly axisymmetric even though the pressure distribution is still not axisymmetric. The pressure and axial velocity distributions approximately two diameters upstream of the outflow boundary, shown in Figs. 16 and 17, respectively, indicated the flow to be axisymmetric at this location. Needless to say, the flow field in the slot was axisymmetric, as can be seen from the pressure distribution at the slot bottom shown in Fig. 18, and has no circumferential velocities or pressure gradients.

Case II Results: As the results of the Case I simulation indicated no asymmetric effects on the flow field in the slot, the boundary condition at the outflow was maintained the same during Case II calculations. In addition, a 7.5° section of the castable inhibitor at one end of the diametral symmetry plane (i.e., at $\theta = +90^\circ$) was assumed to be absent. The computational domain includes only a 180° section ($-90^\circ \leq \theta \leq +90^\circ$) of the SRB (due to symmetry), this corresponds to a failure of a 15° section of the castable inhibitor. The pressure and axial velocity at the outflow plane are shown in Figs. 19 and 20, respectively, which show the asymmetry imposed and the outflow boundary. The pressure and velocity distribution approximately two diameters upstream of the outflow plane, presented in Figs. 21 and 22, respectively, show that the effect of the asymmetry at the outflow boundary does not propagate more than two diameters upstream. Since, in this case, the broken castable inhibitor section also originated asymmetry in the slot, the flow field in the slot was observed to be asymmetric. The pressure distribution at the slot mid-section, shown in Fig. 23, indicates the maximum pressure differential along the circumferential direction to be approximately 1 psi. The pressure reaches a minimum value at $\theta = -30^\circ$ (i.e. 120° away from the location of inhibitor failure) and a maximum value at a location diametrically opposite to the inhibitor failure (i.e. at $\theta = -90^\circ$). The velocity vectors in the r - θ plane at slot mid-section are shown in Fig. 24, with the details of the region near the inhibitor failure being presented in Fig. 25.

Conclusions

An efficient Navier-Stokes analysis has been successfully applied to simulate the complex flow field in the vicinity of a slot in a solid rocket

motor with segment joints. The capability of the computer code to resolve the flow near solid surfaces without using a "wall function" assumption has been demonstrated. In view of the complex nature of the flow field in the vicinity of the slot, this approach is considered essential. The results obtained from these calculations provide valuable design information, which would otherwise be extremely difficult (if not impossible) to obtain. The results of the axisymmetric calculations indicate the presence of a region of reversed axial flow at the aft-edge of the slot and show the over-pressure in the slot to be only about 10 psi. The results of the asymmetric calculations indicate that a pressure asymmetry more than two diameters downstream of the slot has no noticeable effect on the flow field in the slot. They also indicate that the circumferential pressure differential caused in the slot due to failure of a 15° section of the castable inhibitor will be approximately 1 psi.

REFERENCES

1. Sabnis, J.S., Gibeling, H.J. and McDonald, H.: Calculation of Solid Propellant Rocket Motor Internal Flow Field Using an Implicit Navier-Stokes Procedure, AIAA Paper 85-1625, 1985.
2. Dunlap, R., et al: Internal Flow Field Investigation, Air Force Rocket Propulsion Laboratory, Final Report, Contract No. F04611-83-C-0003, November 1986.
3. Jones, W.P. and Launder, B.E.: The Prediction of Laminarization with a Two-Equation Model of Turbulence, Int. J. Heat and Mass Transfer, Vol. 15, pp. 301-314, 1972.
4. Harlow, F.H. and Nakayama, P.I.: Turbulent Transport Equations, Phys. Fluids, Vol. 10, No. 11, pp. 2323-2332, 1967.
5. Briley, W.R. and McDonald, H.: Solution of the Multidimensional Compressible Navier-Stokes Equations by a Generalized Implicit Method, Journal of Comp. Physics, Vol. 24, pp. 372-397, August 1977.
6. Douglas, J. and Gunn, J.E.: A General Formulation of Alternating Direction Methods, Part I, "Parabolic and Hyperbolic Problems", Numerische Mathematik, Vol. 6, p. 428-453, 1964.
7. Briley, W.R. and McDonald, H.: On the Structure and Use of Linearized Block Implicit Schemes. J. Comp. Physics, Vol. 34, No. 1, pp. 54-72, January 1980.
8. Culick, F.E.C.: Rotational Axisymmetric Mean Flow and Damping of Acoustic Waves in a Solid Propellant Rocket, AIAA Journal, Vol. 4, No. 8, pp. 1462-1469, August 1966.
9. Oh, Y.H.: An Analytical Transformation Technique for Generating Uniformly Spaced Computational Mesh. Final Report, NASA Langley Research Grant NSF 1087, October 1978.

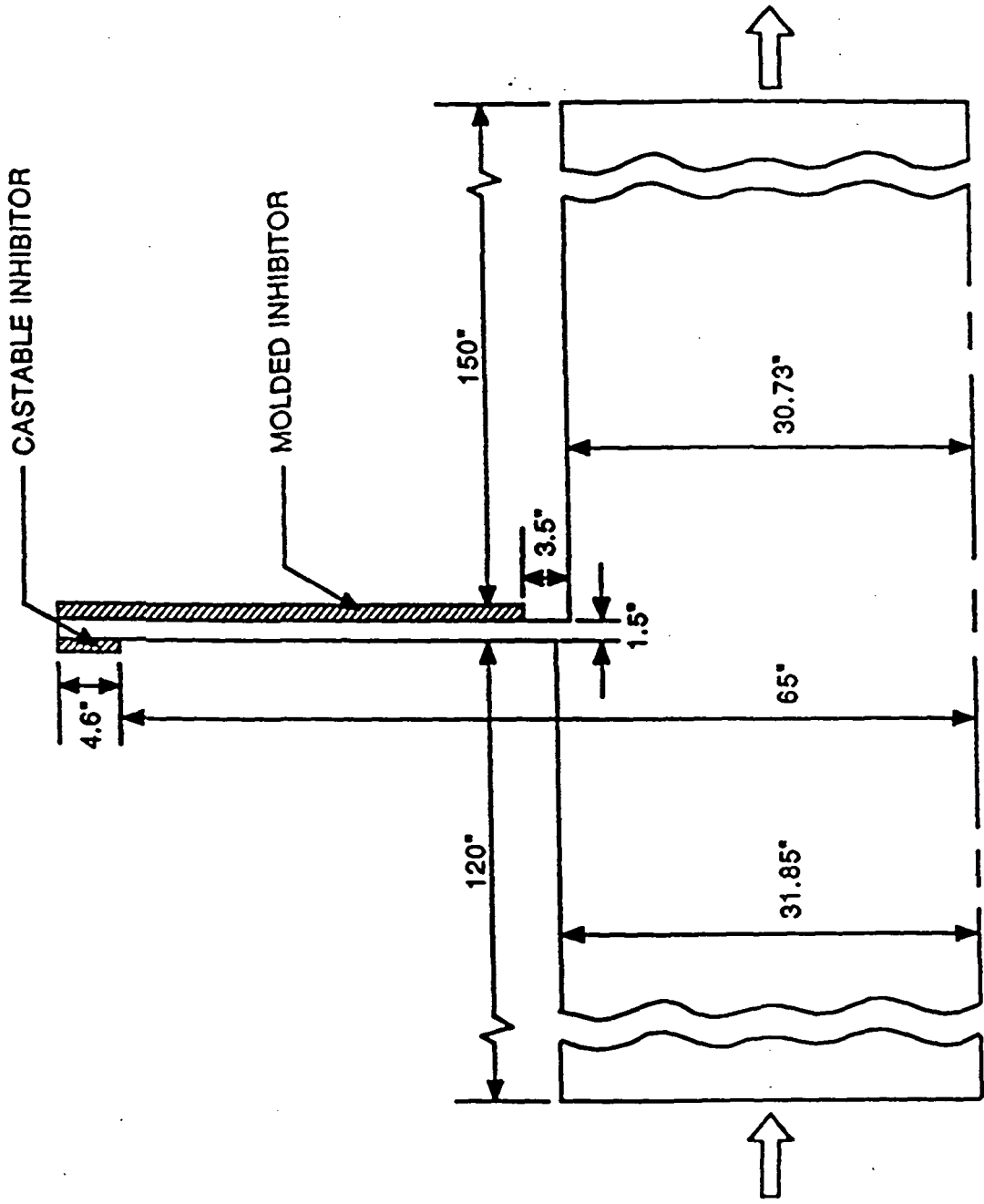


Fig. 1 - Computational Domain for Axisymmetric Calculations

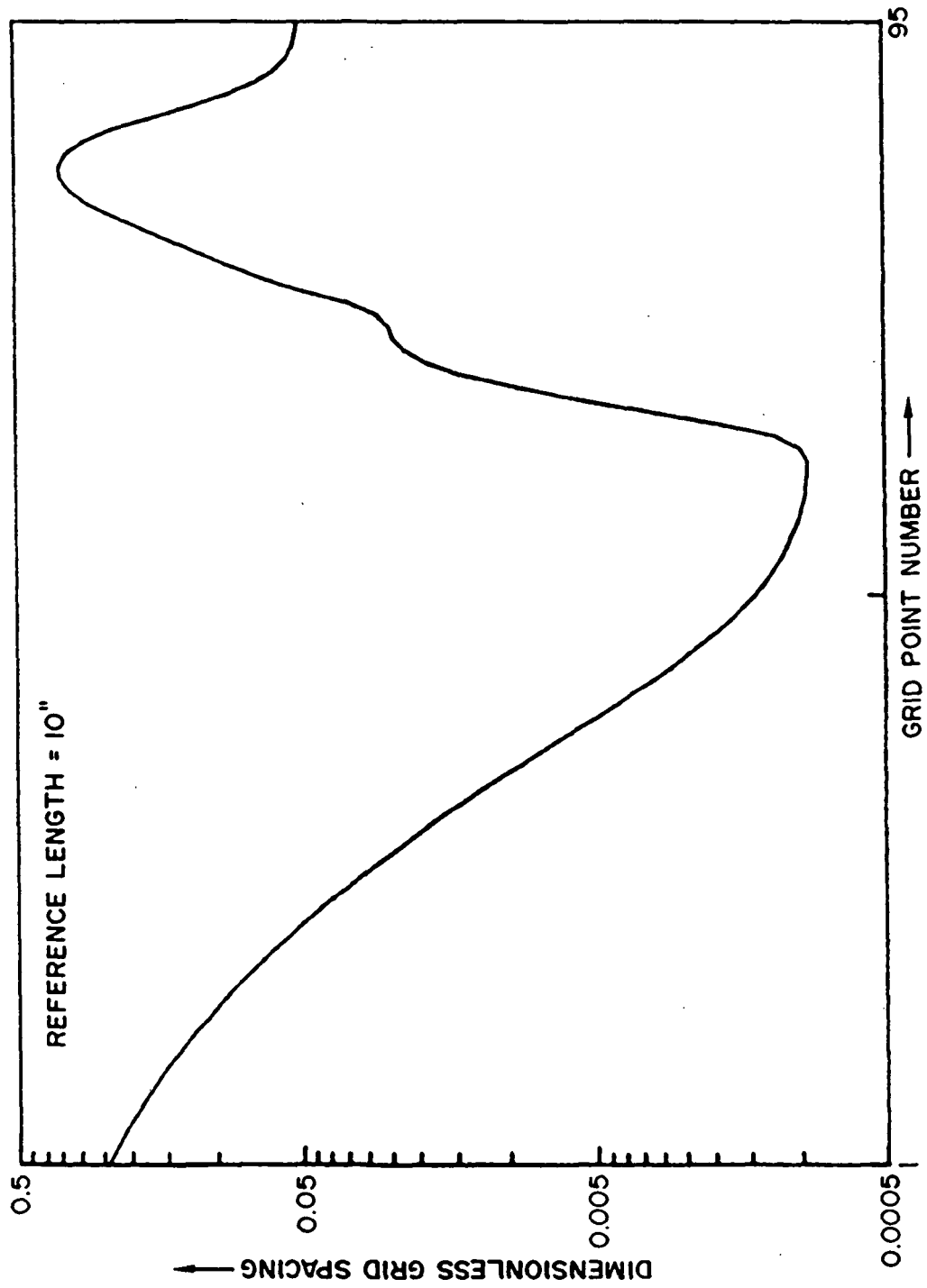


Fig. 2 - Grid Distribution along Radial Direction

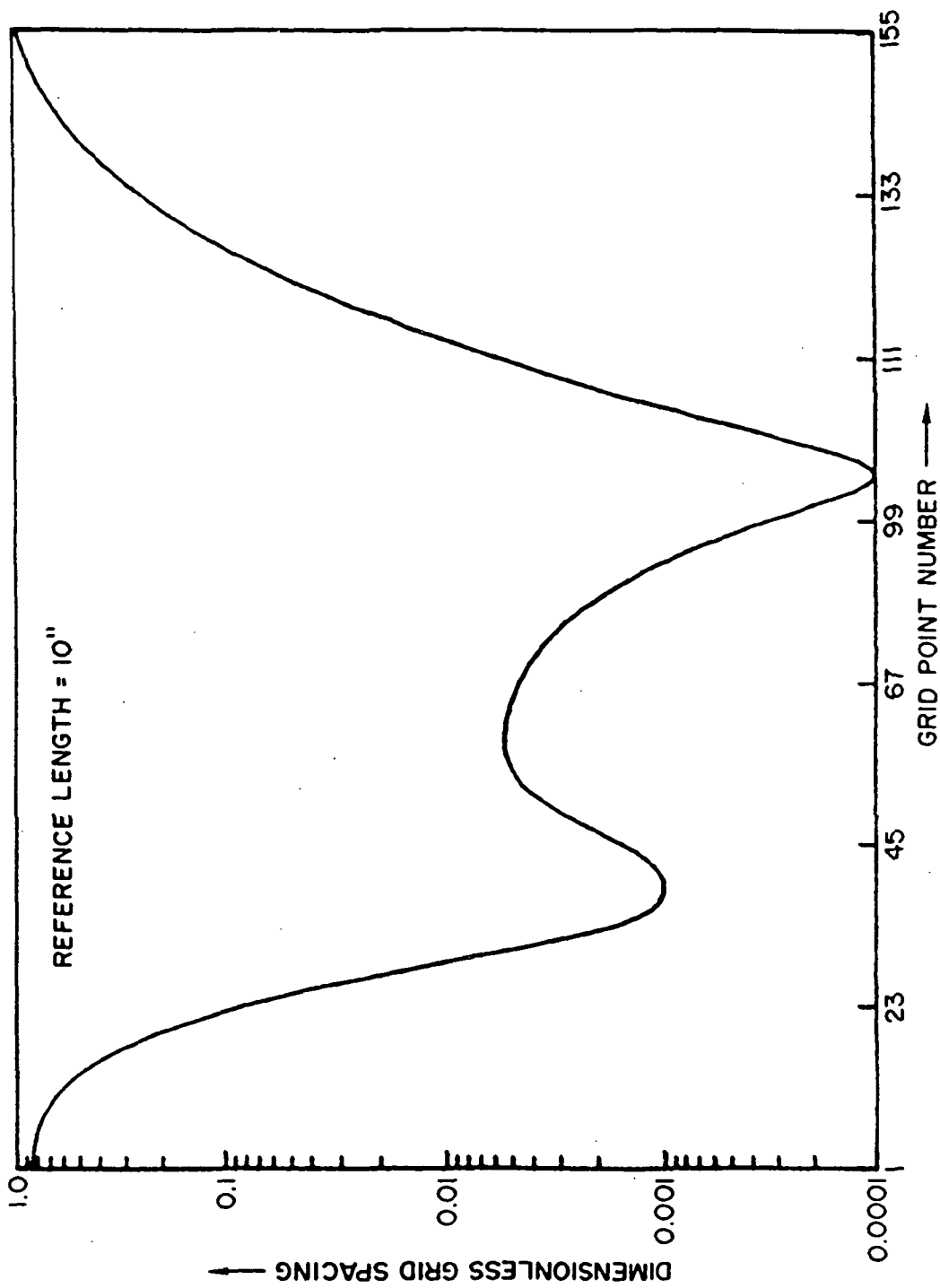


Fig. 3 - Grid Distribution along Axial Direction

GRID

95x155 GRID

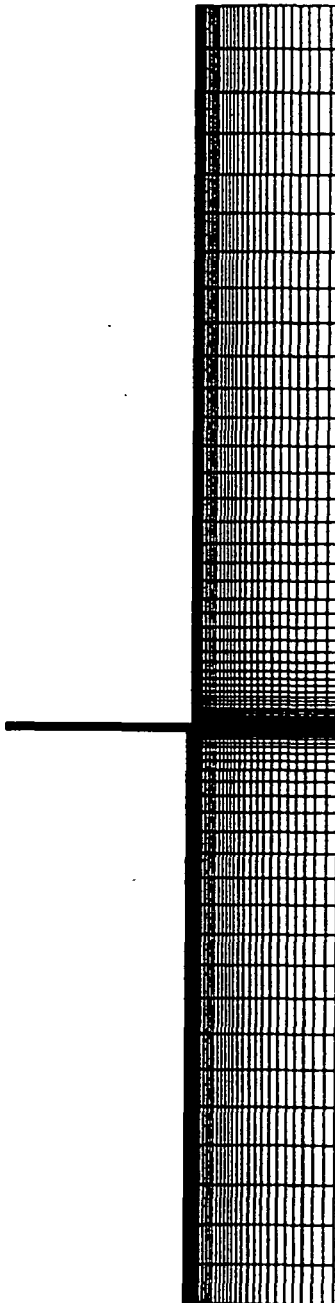


Fig. 4 - Computational Grid in r-z Plane

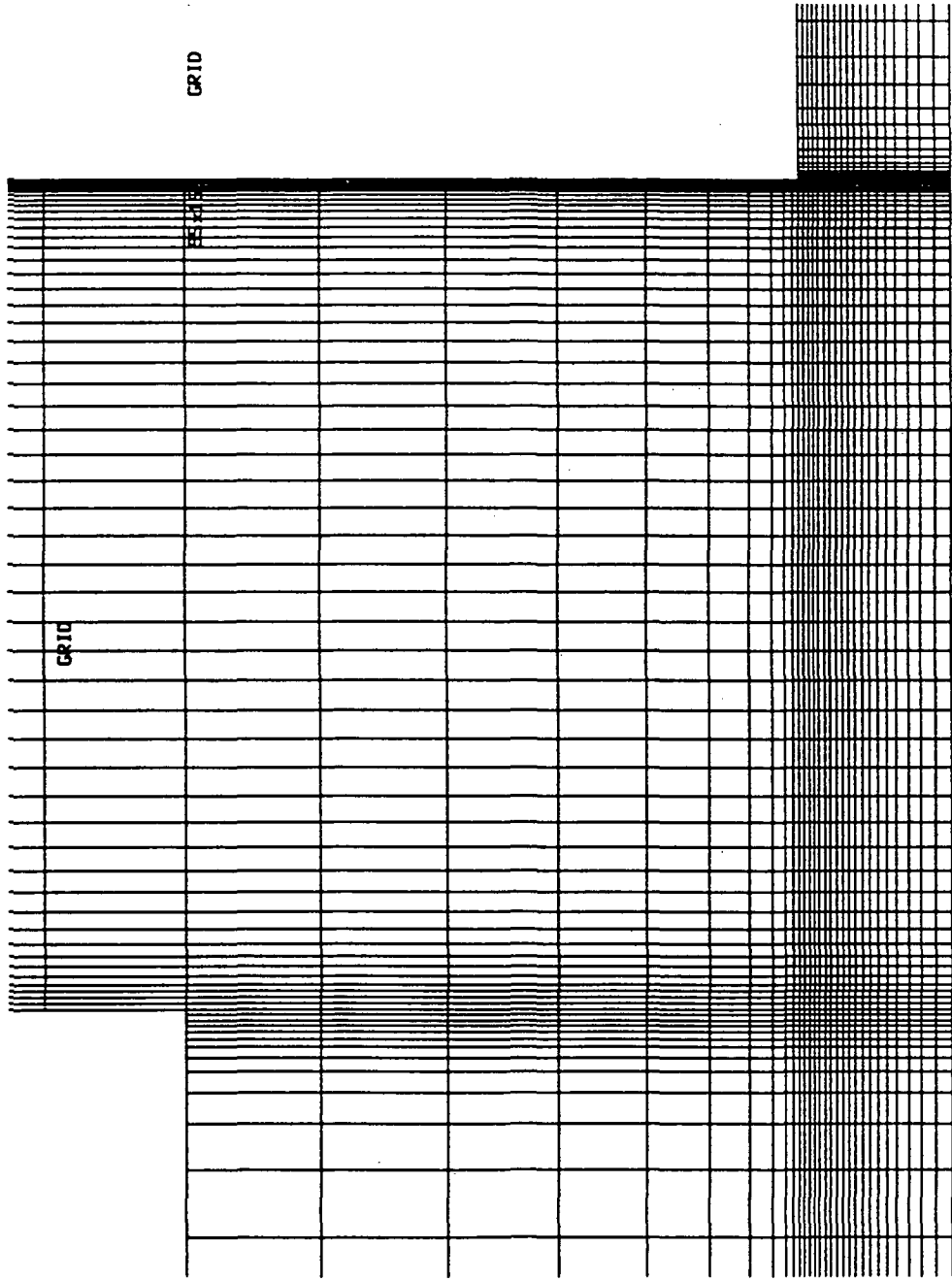


Fig. 5 -- Details of the Grid Near Slot Exit

ORIGINAL PAGE IS
OF POOR QUALITY

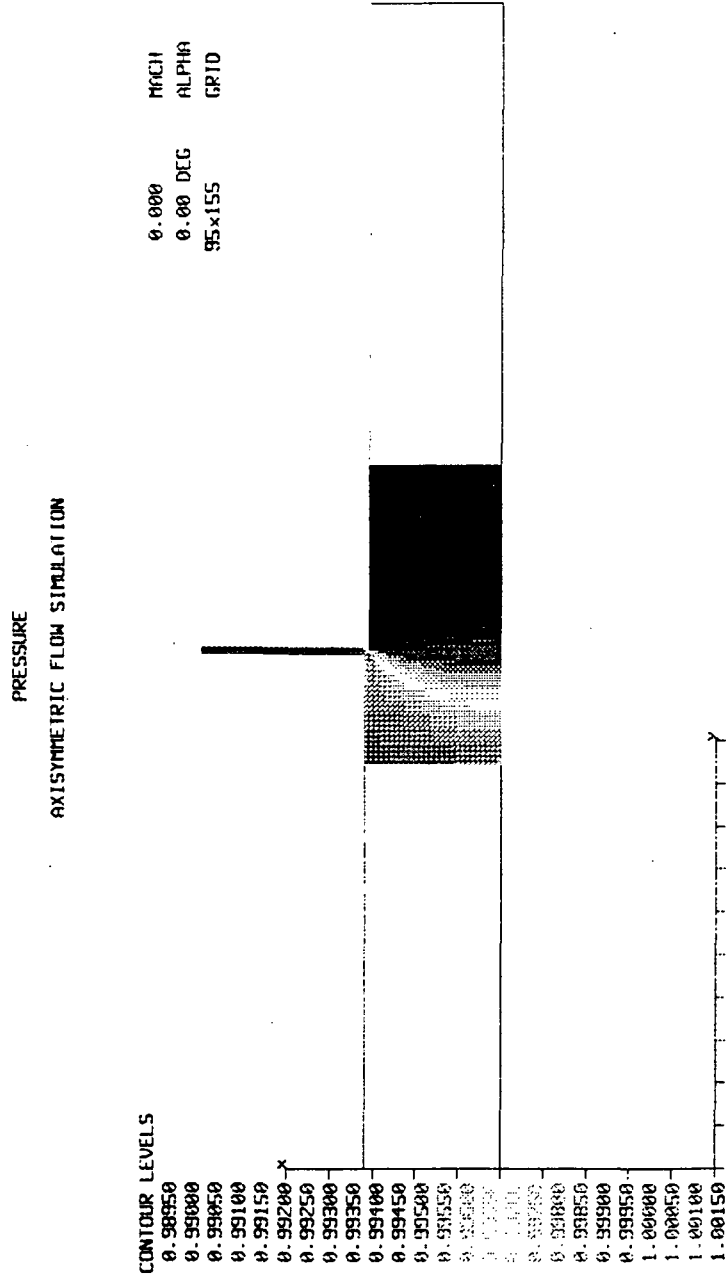


Fig. 6 - Pressure Distribution in the Chamber

ORIGINAL PAGE IS
OF POOR QUALITY

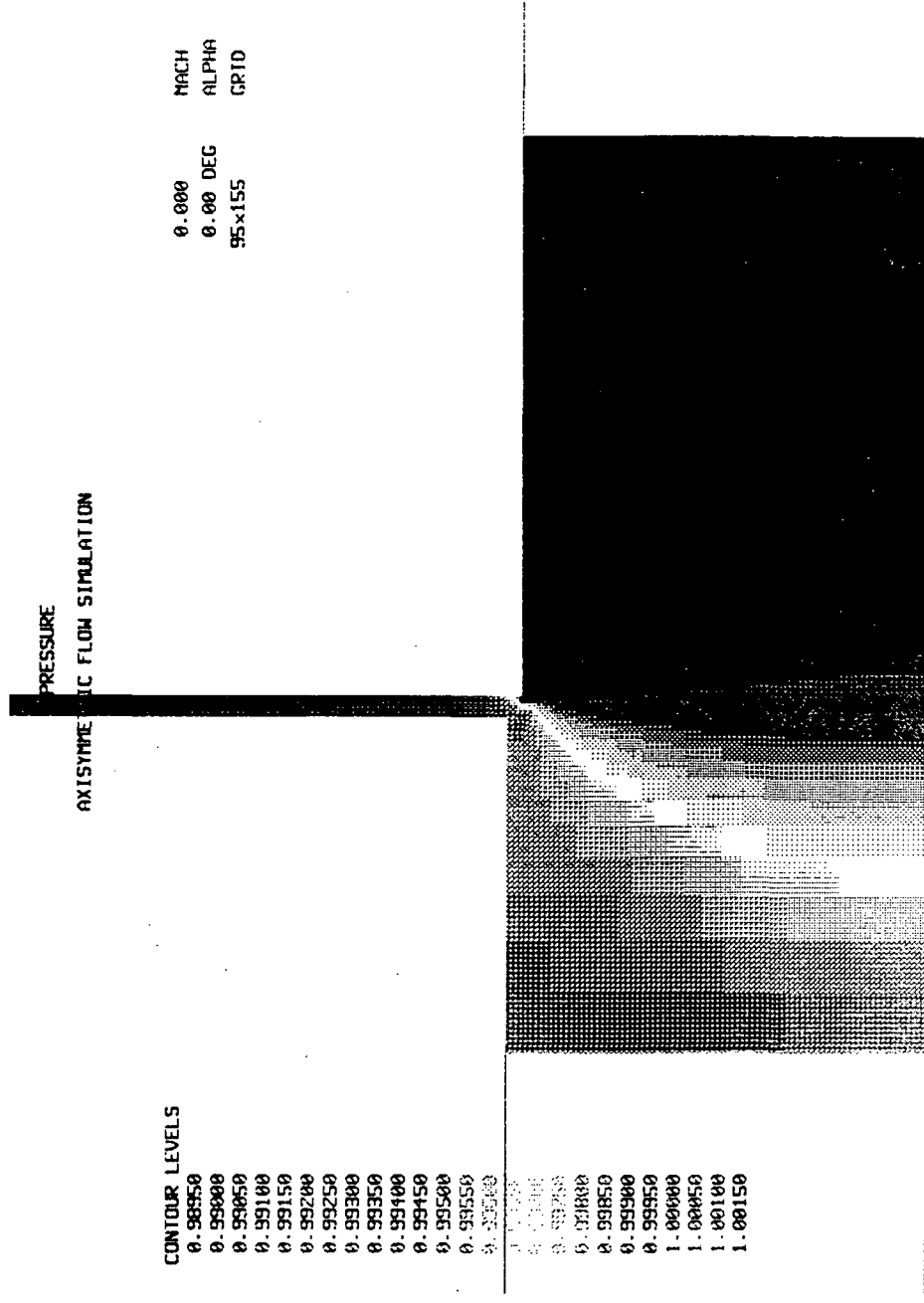


Fig. 7 - Pressure Distribution in the Vicinity of the Slot

ORIGINAL PAGE IS
OF POOR QUALITY

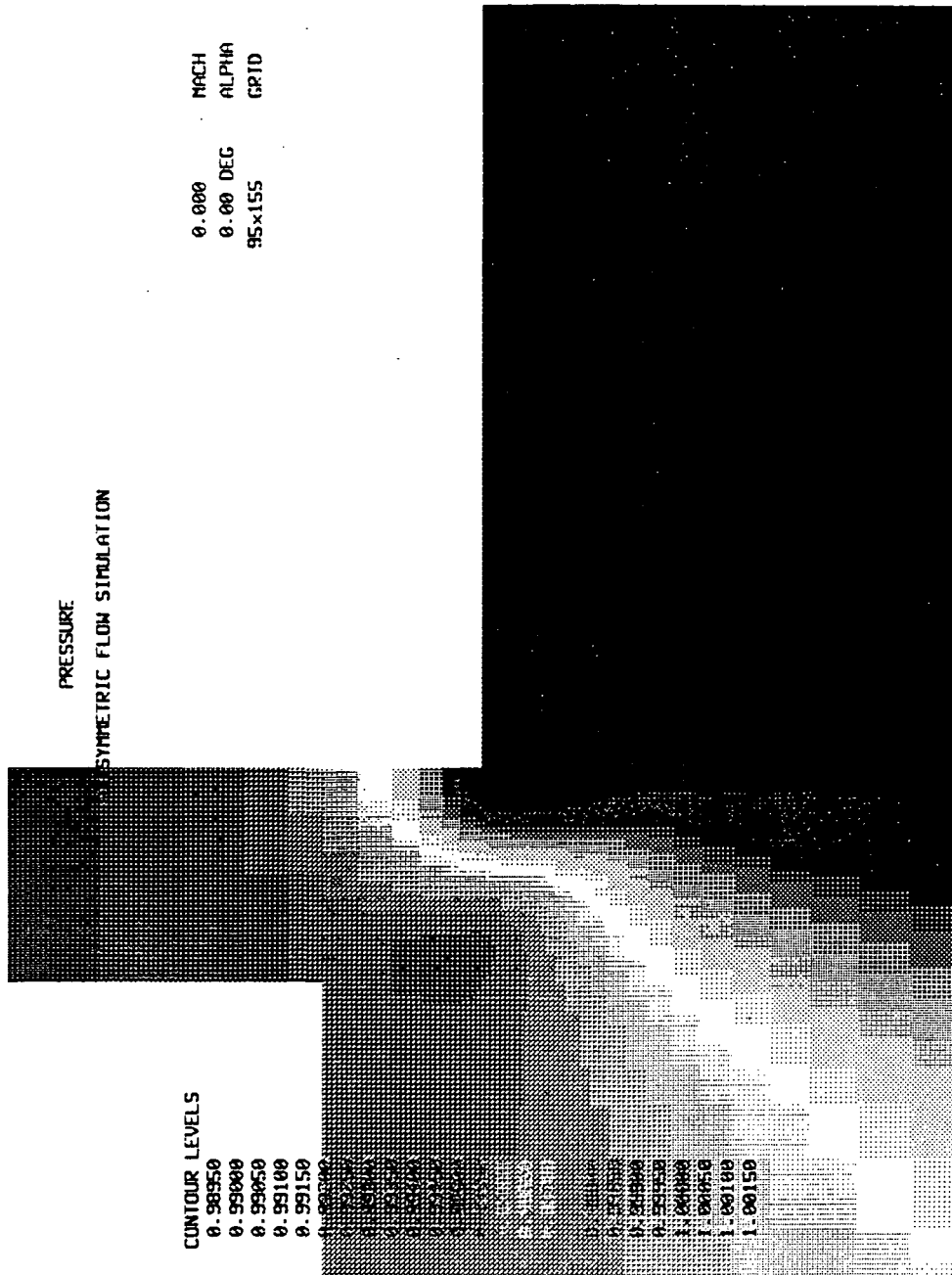


Fig. 8 - Pressure Distribution Near Slot Exit

ORIGINAL PAGE IS
OF POOR QUALITY.

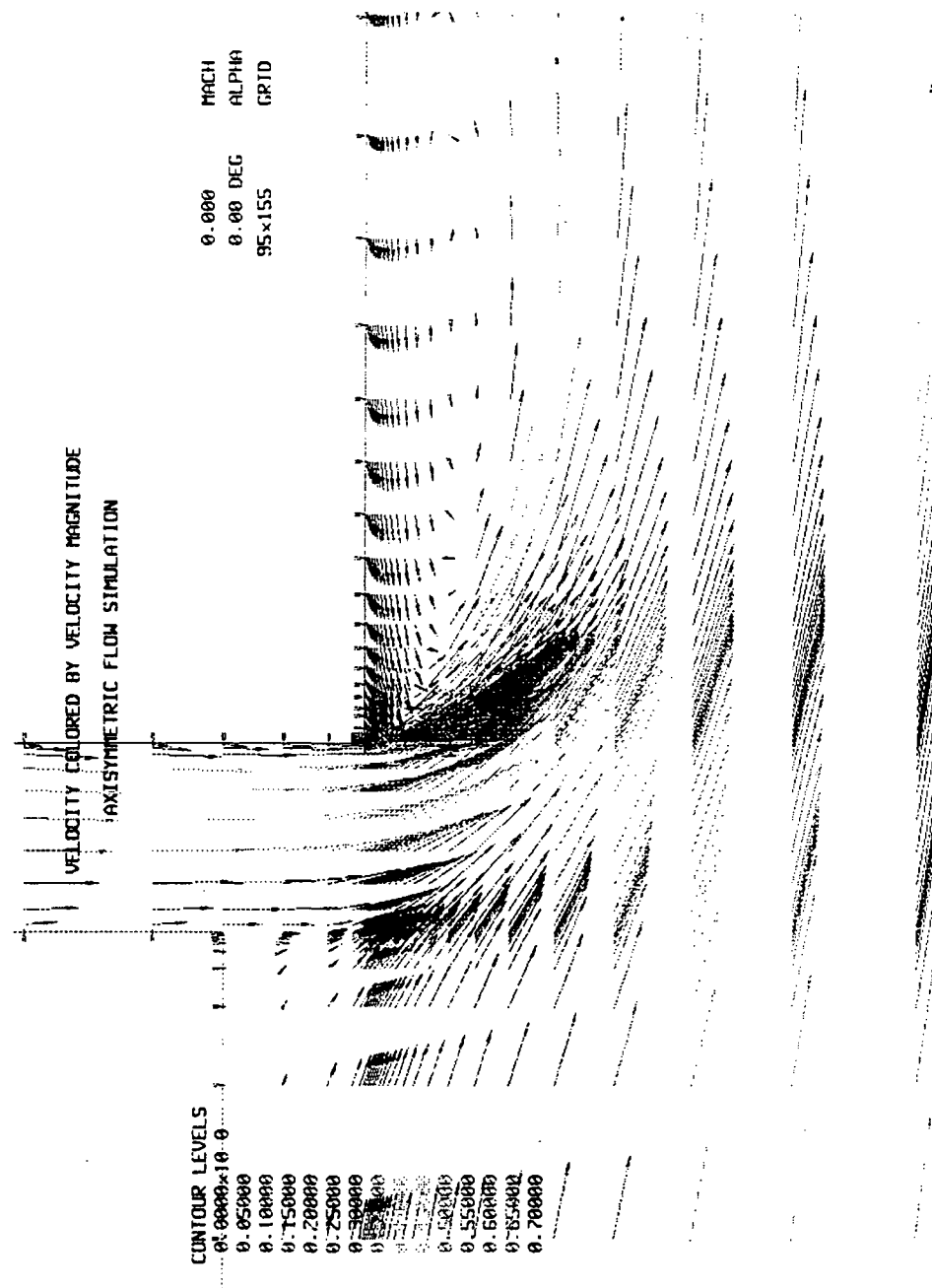


Fig. 9 - Velocity Vectors Near Slot Exit

ORIGINAL PAGE IS
OF POOR QUALITY

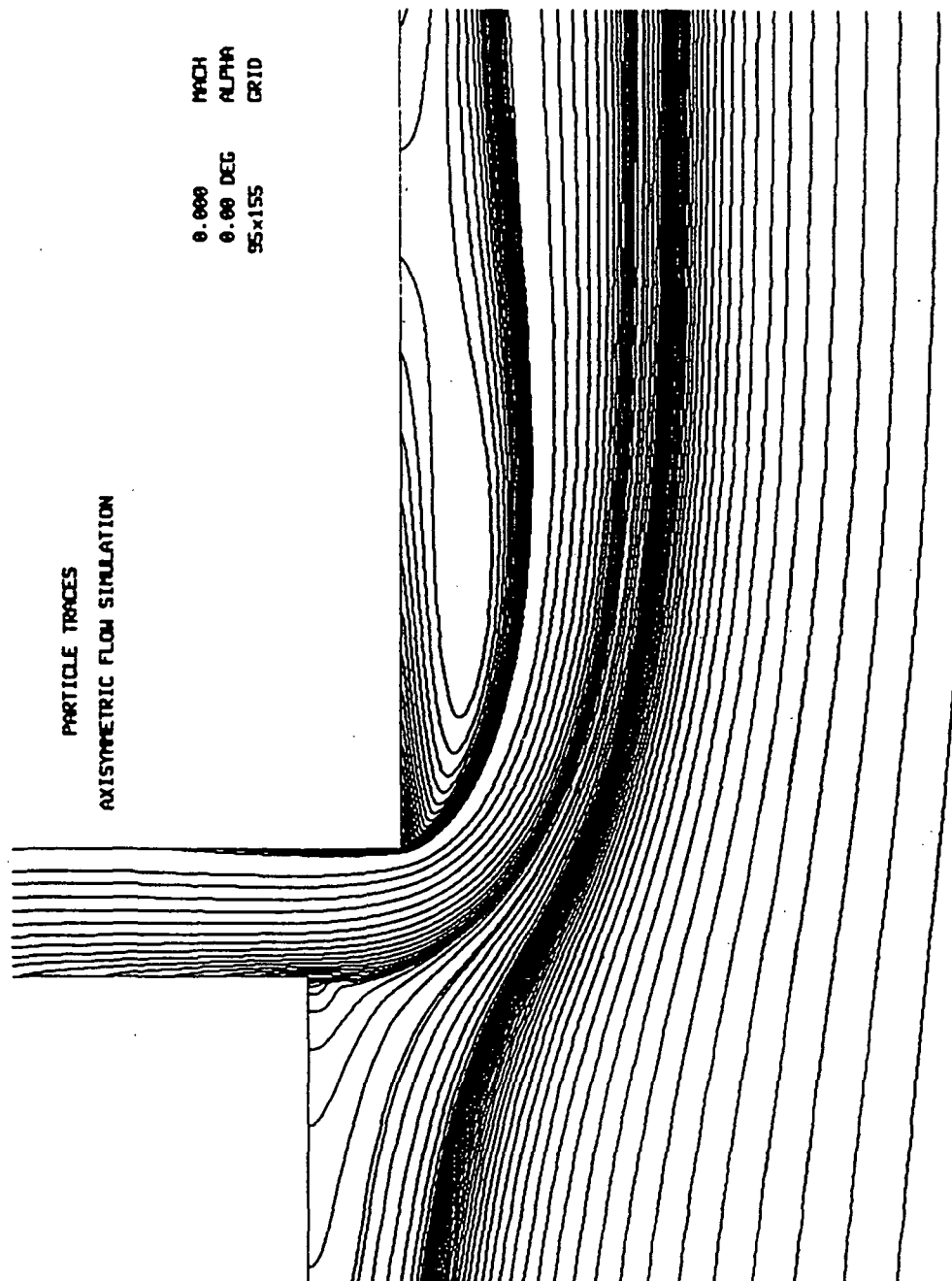


Fig. 10 - Streaklines Near Slot Exit

ORIGINAL PAGE IS
OF POOR QUALITY

PRESSURE
ASYMMETRIC FLOW - CASE 1
OUT-FLOW BOUNDARY

CONTOUR LEVELS

0.98300
0.98350
0.98400
0.98450
0.98500
0.98550
0.98600
0.98650
0.98700
0.98750
0.98800
0.98850
0.98900
0.98950
0.99000
0.99050
0.99100
0.99150
0.99200
0.99250
0.99300
0.99350
0.99400

0.000
0.00 DEG
48x49x53
MACH
ALPHA
GRID

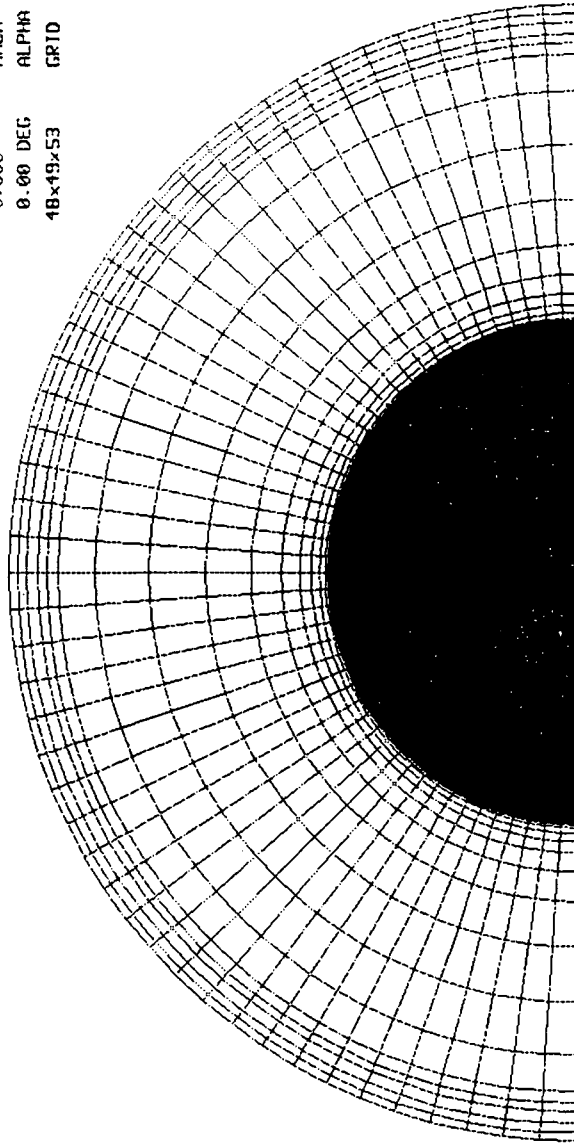


Fig. 12 - Pressure Distribution at Outflow Boundary

ORIGINAL PAGE IS
OF POOR QUALITY

W VELOCITY
ASYMMETRIC FLOW - CASE 1
OUT-FLOW BOUNDARY

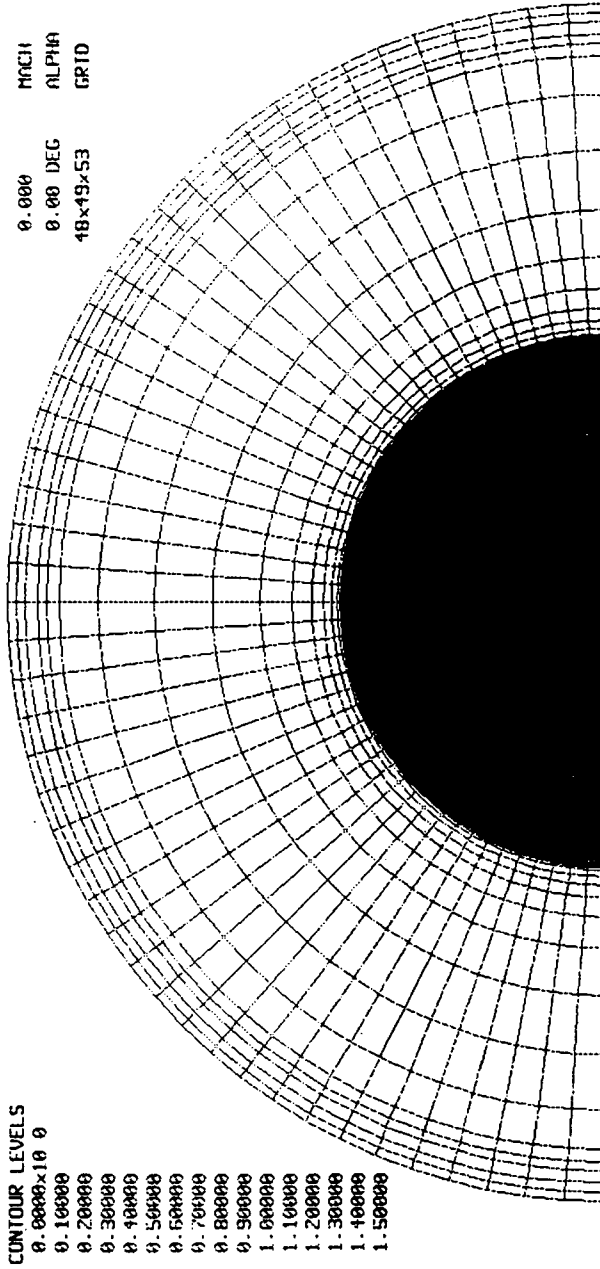


Fig. 13 - Axial Velocity Distribution at Outflow Boundary

ORIGINAL PAGE IS
OF POOR QUALITY

PRESSURE
ASYMMETRIC FLOW - CASE 1
ONE-DIAMETER UPSTREAM OF OUT-FLOW BOUNDARY

CONTOUR LEVELS
0.99270
0.99275
0.99280
0.99285
0.99290
0.99295
0.99300
0.99305
0.99310
0.99315
0.99320
0.99325
0.99330
0.99335
0.99340
0.99345
0.99350
0.99355
0.99360

0.000
0.00 DEG
48x49x53
GRID

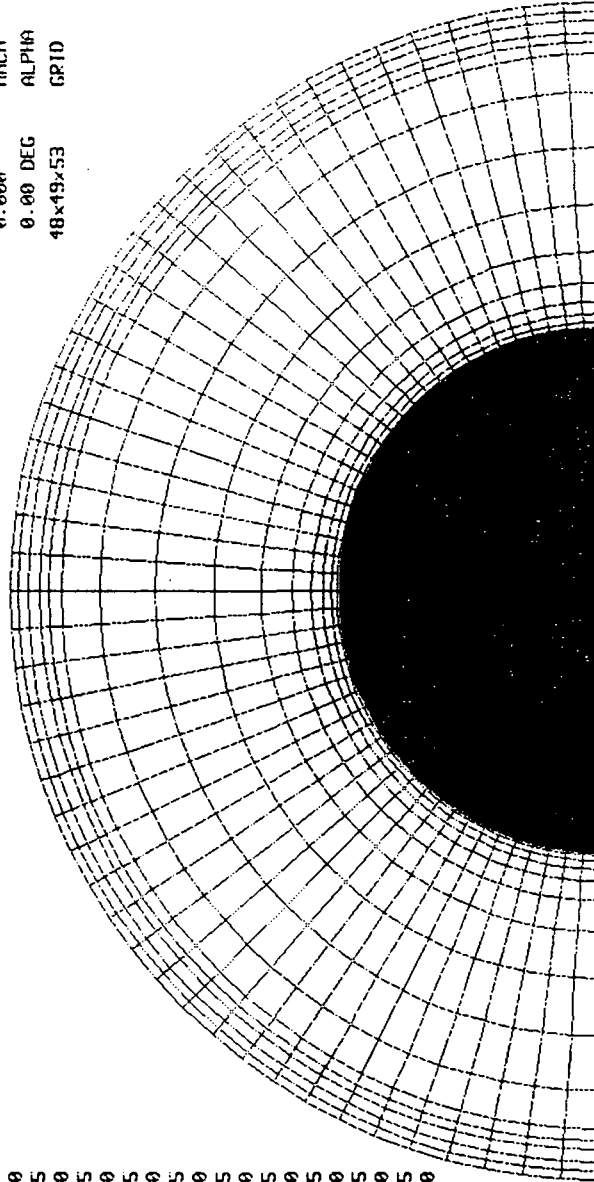
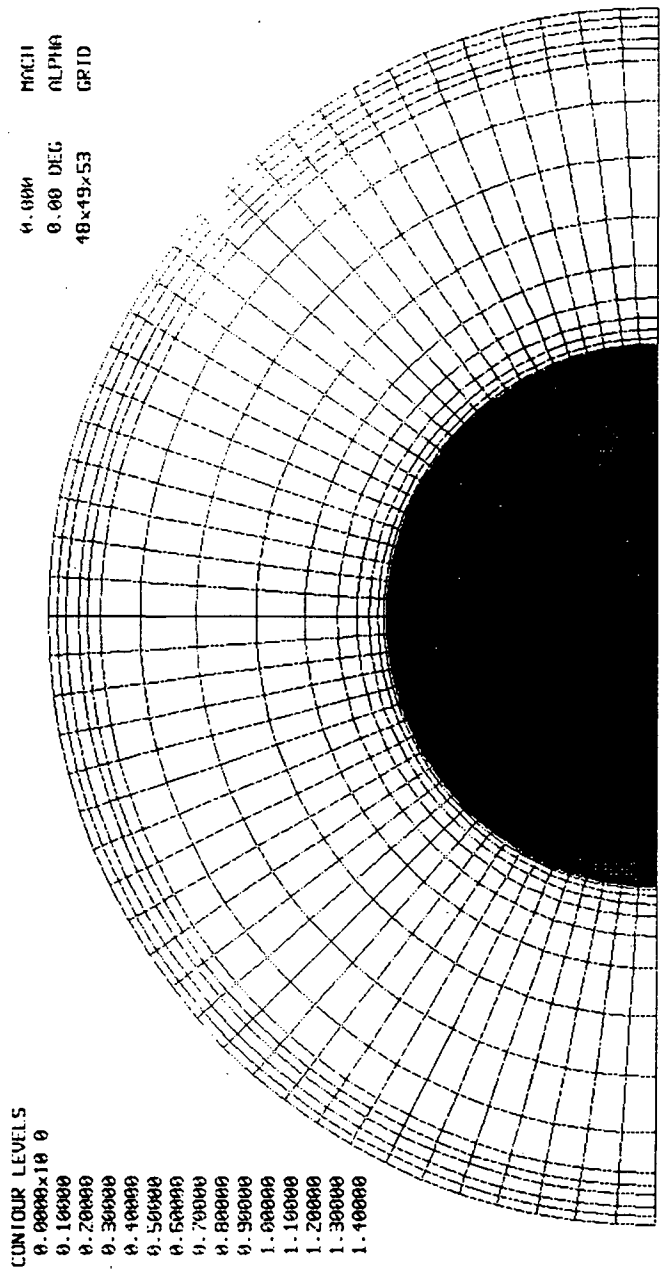


Fig. 14 - Pressure Distribution One Diameter Upstream of Outflow Boundary

ORIGINAL PAGE IS
OF POOR QUALITY

U VELOCITY
ASYMMETRIC FLOW - CASE 1
ONE-DIAMETER UPSTREAM OF OUT-FLOW BOUNDARY



CONTOUR LEVELS
0.0000x10 0
0.10000
0.20000
0.30000
0.40000
0.50000
0.60000
0.70000
0.80000
0.90000
1.00000
1.10000
1.20000
1.30000
1.40000

U: 0.000
MACH: 0.00 DEG
ALPHA: 48x49x53
GRID

Fig. 15 - Axial Velocity Distribution One Diameter Upstream of Outflow Boundary

ORIGINAL PAGE IS
OF POOR QUALITY

PRESSURE
ASYMMETRIC FLOW - CASE 1
TWO-DIAMETERS UPSTREAM OF OUT-FLOW BOUNDARY

CONTOUR LEVELS
0.99852
0.99854
0.99856
0.99858
0.99860
0.99862
0.99864
0.99866
0.99868
0.99870
0.99872
0.99874
0.99876
0.99878
0.99880
0.99882

0.000
0.00 DEG
48x49x53
MACH
ALPHA
GRID

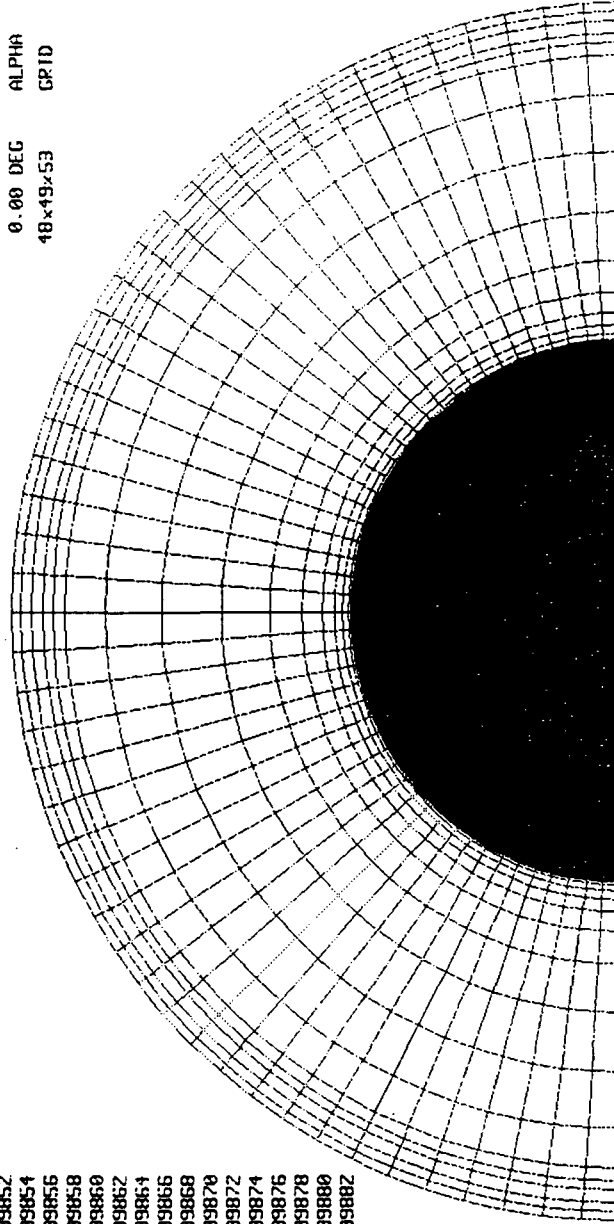
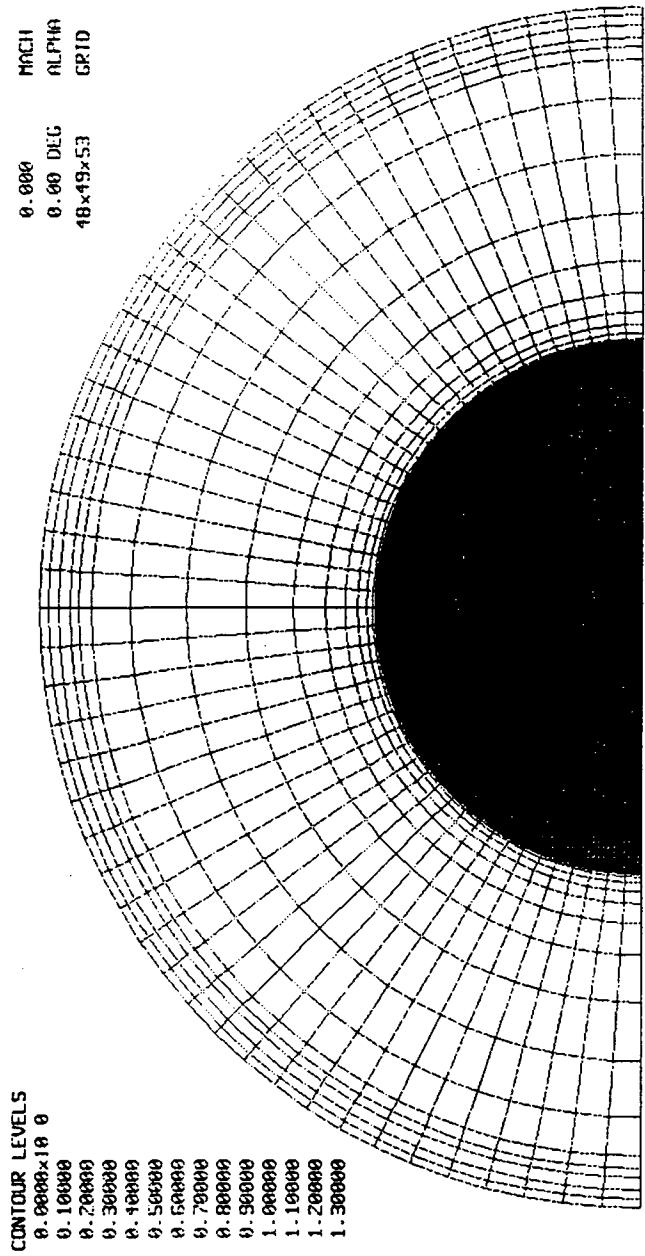


Fig. 16 - Pressure Distribution Two Diameters Upstream of Outflow Boundary

ORIGINAL PAGE IS
OF POOR QUALITY

W VELOCITY
ASYMMETRIC FLOW - CASE 1
TWO-DIAMETERS UPSTREAM OF OUT-FLOW BOUNDARY



CONTOUR LEVELS
0.0000x10 0
0.10000
0.20000
0.30000
0.40000
0.50000
0.60000
0.70000
0.80000
0.90000
1.00000
1.10000
1.20000
1.30000

0.000 MACH
0.00 DEG ALPHA
48x49x53 GRID

Fig. 17 - Axial Velocity Distribution Two Diameters Upstream of Outflow Boundary

ORIGINAL PAGE IS
OF POOR QUALITY

PRESSURE
ASYMMETRIC FLOW - CASE 1
SLOT MID-SECTION

CONTOUR LEVELS

- 1.00952
- 1.00954
- 1.00956
- 1.00958
- 1.00960
- 1.00962
- 1.00964
- 1.00966
- 1.00968
- 1.00970
- 1.00972
- 1.00974
- 1.00976
- 1.00978
- 1.00980
- 1.00982
- 1.00984
- 1.00986
- 1.00988

- 0.000
- 0.00 DEG
- 48x49x53
- MMCH
- ALPHA
- GRID

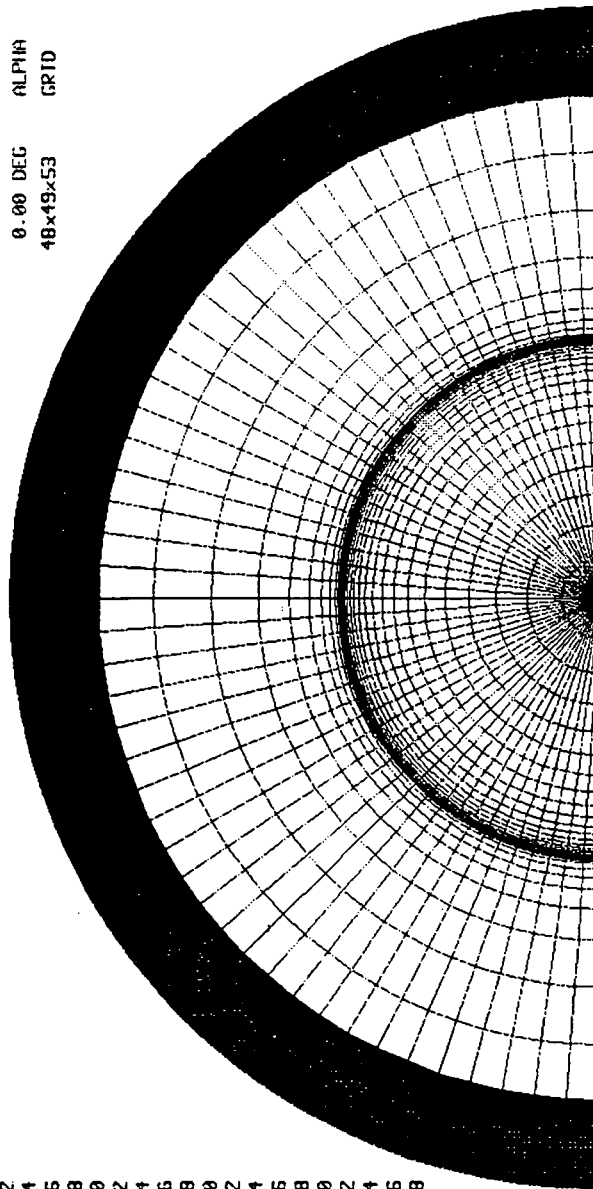


Fig. 18 - Pressure Distribution at Slot Mid-Section

ORIGINAL PAGE IS
OF POOR QUALITY

PRESSURE
ASYMMETRIC FLOW - CASE II
OUT-FLOW BOUNDARY

CONTOUR LEVELS

0.98380
0.98350
0.98400
0.98450
0.98500
0.98550
0.98600
0.98700
0.98750
0.98800
0.98850
0.98900
0.98950
0.99000
0.99050
0.99100
0.99150
0.99200
0.99250
0.99300
0.99350
0.99400

0.000 MACH
0.00 DEG ALPHA
18x49x53 GRID

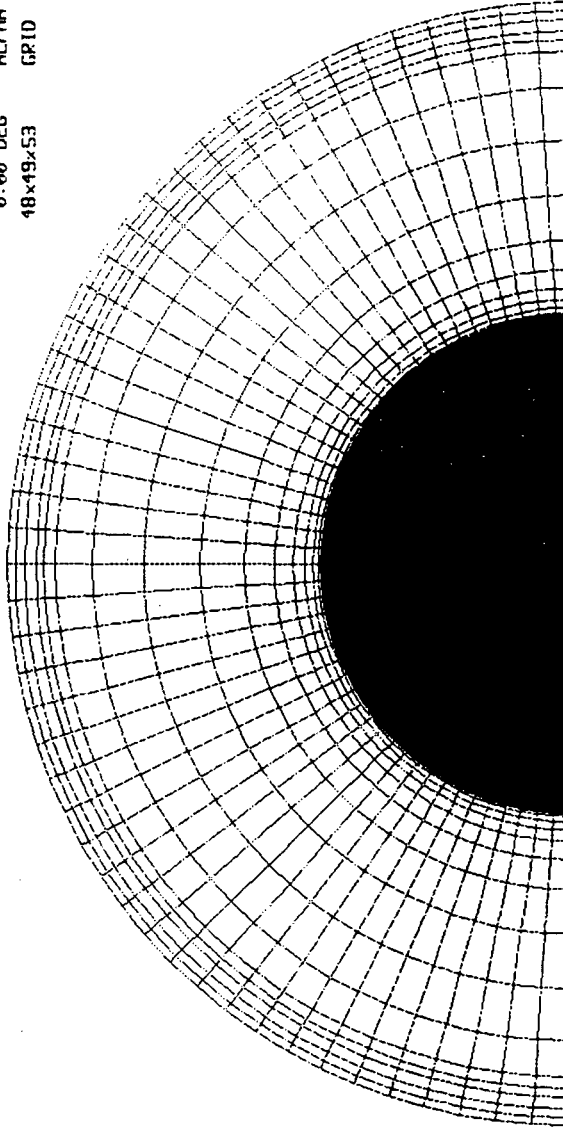


Fig. 19 - Pressure Distribution at Outflow Boundary (Case II)

ORIGINAL PAGE IS
OF POOR QUALITY

U VELOCITY
ASYMMETRIC FLOW - CASE II
OUT-FLOW BOUNDARY

CUNTOUR LEVELS
0.0000x10 0
0.10000
0.20000
0.30000
0.40000
0.50000
0.60000
0.70000
0.80000
0.90000
1.00000
1.10000
1.20000
1.30000
1.40000
1.50000

0.000
0.00 DEG
48x49x53
MOCII
ALP110
GPTD

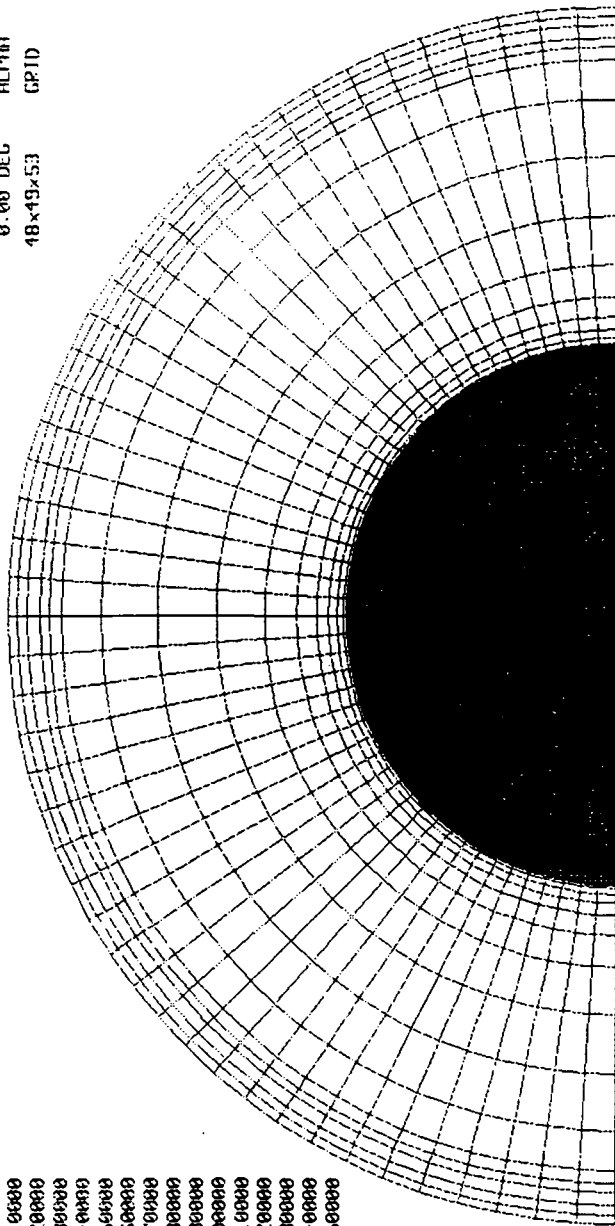


Fig. 20 - Axial Velocity Distribution at Outflow Boundary (Case II)

ORIGINAL PAGE IS
OF POOR QUALITY

PRESSURE
ASYMMETRIC FLOW - CASE II
TWO-DIAMETERS UPSTREAM OF OUT-FLOW BOUNDARY

CONTOUR LEVELS

0.99510
0.99512
0.99514
0.99516
0.99518
0.99520
0.99522
0.99524
0.99526
0.99528
0.99530
0.99532
0.99534
0.99536
0.99538
0.99540
0.99542
0.99544
0.99546
0.99548
0.99550
0.99552
0.99554
0.99556
0.99558
0.99560
0.99562
0.99564
0.99566
0.99568
0.99570
0.99572
0.99574
0.99576
0.99578

0.000 MACH
0.00 DEG ALPHA
48x49x53 GRID

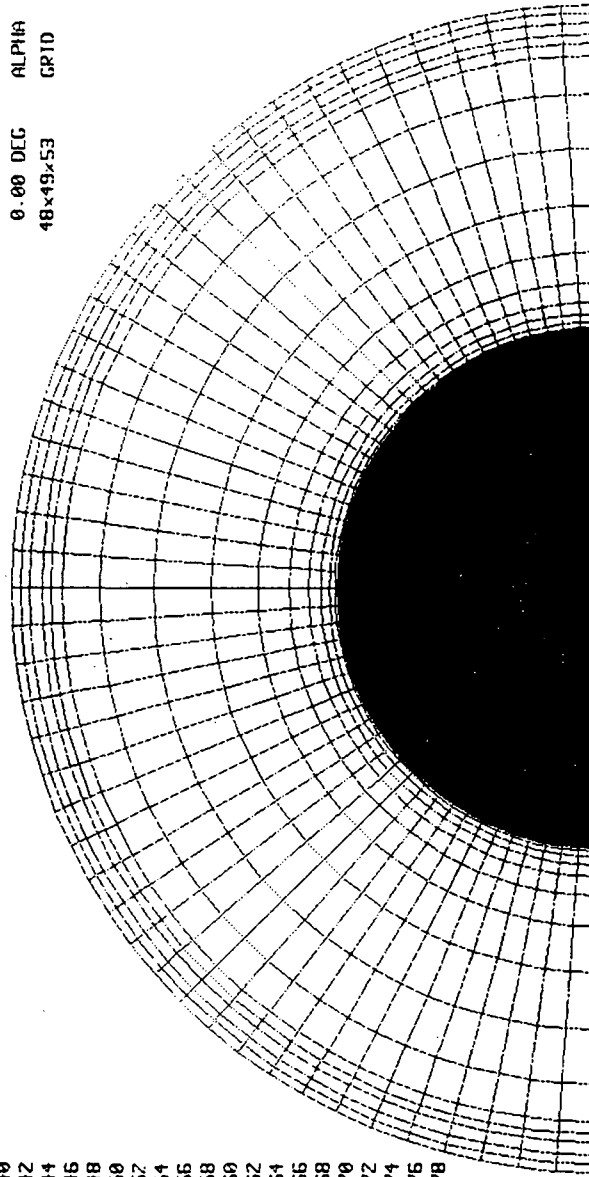


Fig. 21 - Pressure Distribution Two Diameters Upstream of Outflow Boundary (Case II)

ORIGINAL PAGE IS
OF POOR QUALITY

U VELOCITY
ASYMMETRIC FLOW - CASE II
TWO-DIAMETERS UPSTREAM OF OUT-FLOW BOUNDARY

CUNTOUR LEVELS
0.0000x10 0
0.10000
0.20000
0.30000
0.40000
0.50000
0.60000
0.70000
0.80000
0.90000
1.00000
1.10000
1.20000
1.30000

0.000
0.00 DEG
48x49x53
MACH
ALPHA
GRID

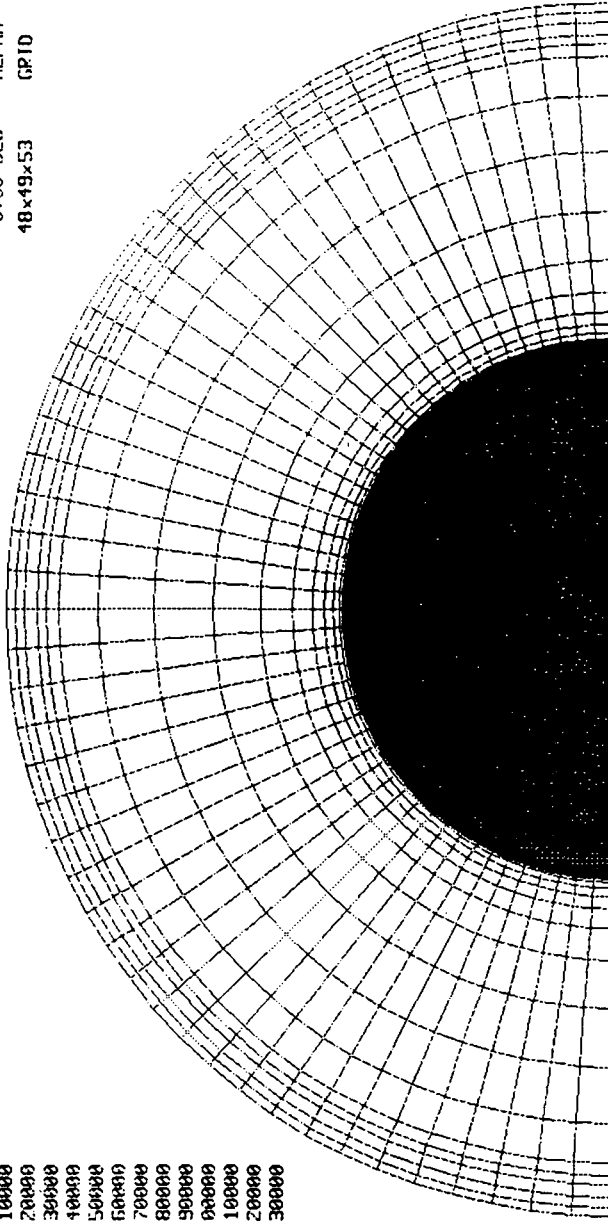


Fig. 22 - Axial Velocity Distribution Two Diameters Upstream of Outflow Boundary (Case II)

PRESSURE
ASYMMETRIC FLOW - CASE II
SLOT MID-SECTION

CONTOUR LEVELS

- 1.00475
- 1.00480
- 1.00485
- 1.00490
- 1.00495
- 1.00500
- 1.00505
- 1.00510
- 1.00515
- 1.00520
- 1.00525
- 1.00530
- 1.00535
- 1.00540
- 1.00545
- 1.00550
- 1.00555
- 1.00560
- 1.00565
- 1.00570
- 1.00575
- 1.00580
- 1.00585
- 1.00590
- 1.00595

0.000 MACH
0.00 DEG ALPHA
48x49x53 GRID

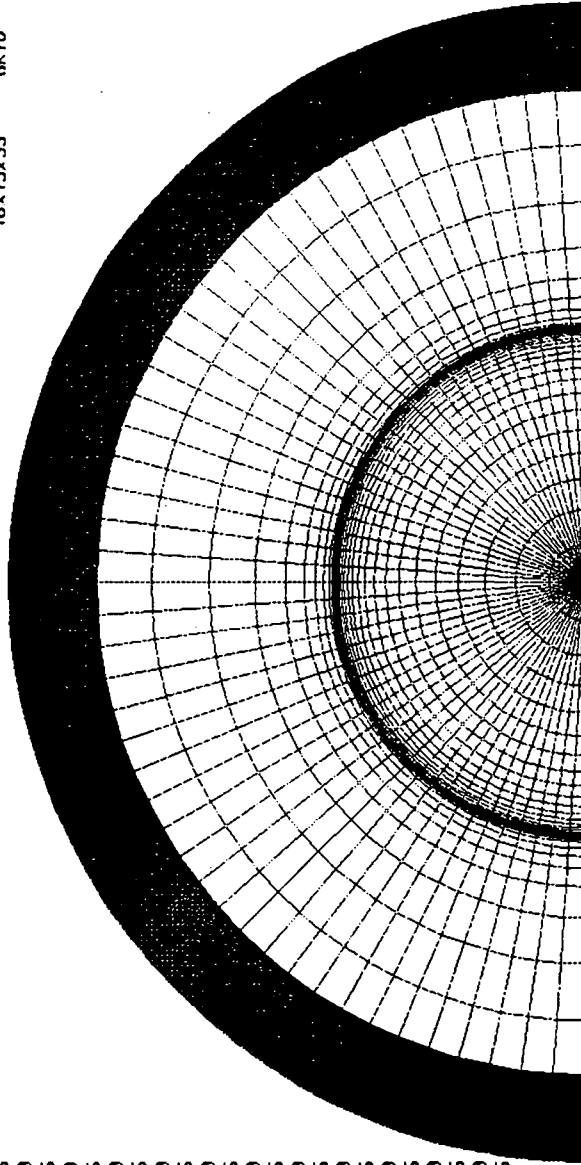


Fig. 23 - Pressure Distribution at Slot Mid-Section (Case II)

ORIGINAL PAGE IS
OF POOR QUALITY

VELOCITY COLORED BY VELOCITY MAGNITUDE
ASYMMETRIC FLOW - CASE II
SLOT MID-SECTION

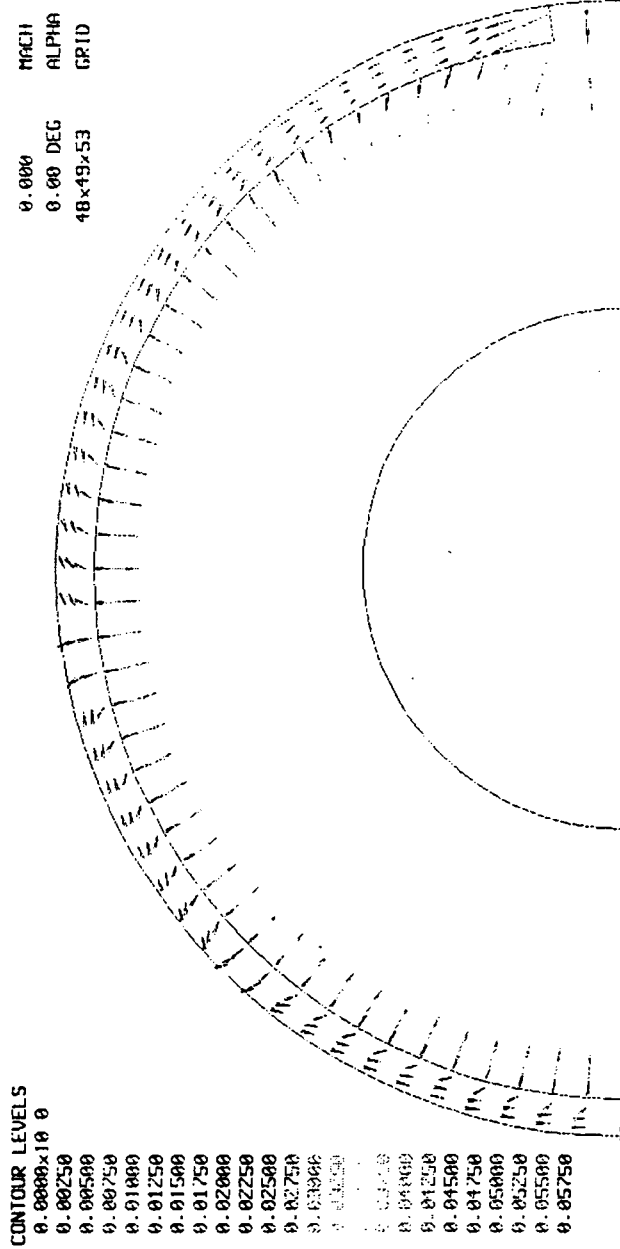


Fig. 24 - Velocity Vectors in r-θ Plane at Slot Mid-Section (Case II)

ORIGINAL PAGE IS
OF POOR QUALITY.

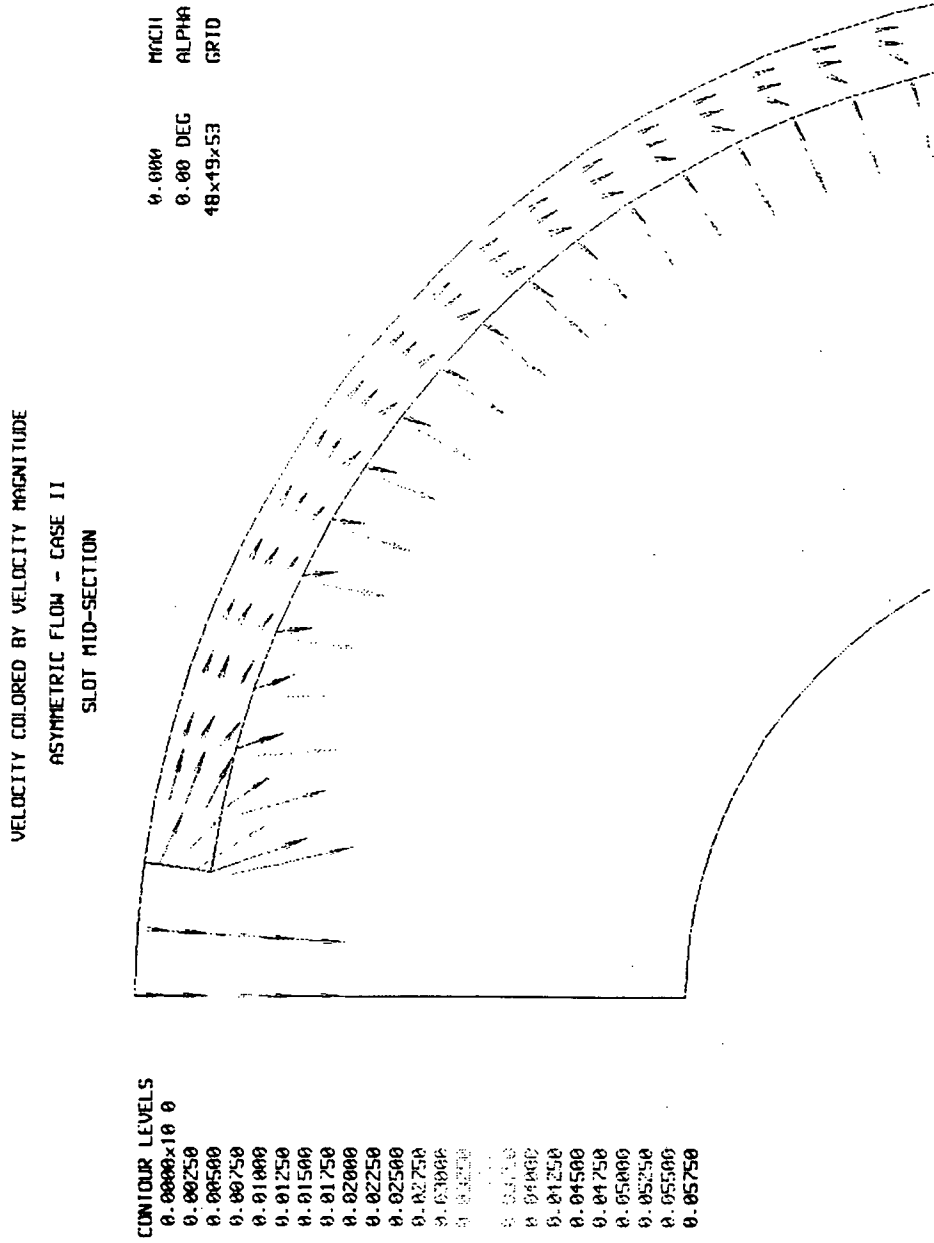


Fig. 25 - Velocity Vectors in r-θ Plane at Near Inhibitor Failure